Monthly Notices
of the
ROYAL ASTRONOMICAL SOCIETY

Mon. Not. R. Astron. Soc. **412,** 1320–1330 (2011) doi:10.1111/j.1365-2966.2010.17989.x

Modelling the equatorial emission in a microquasar

T. Smponias[1,2,4] and T. S. Kosmas[1,3]★

[1]*Physics Department, University of Ioannina, Ioannina, 45110, Greece*
[2]*Department of Informatics and Computer Technology, TEI of Western Macedonia, GR-52100 Kastoria, Greece*
[3]*GSI, Theoretical Physics Division, D-64291 Darmstadt, and Institute of Nuclear Physics, TU Darmstadt, D-64289, Darmstadt, Germany*
[4]*Department of Information Technology and Telecommunication, TEI of Epirus, GR-47100 Arta, Greece*

Accepted 2010 November 7. Received 2010 October 18; in original form 2010 April 24

ABSTRACT

The jets in a microquasar are modelled using a three-dimensional relativistic hydrocode (PLUTO), with the aim of investigating the appearance of equatorial radio emission. A dynamical mechanism is explored whereby the bow shocks of the jets strongly affect the equatorial regions. The presence of an extended disc is assumed and its role proves to be important in producing equatorial emission. As a concrete example, we focus on the SS 433 microquasar, one of the most intensively studied objects in the Galaxy, for which equatorial emission has been repeatedly detected during the last decade.

Key words: radiation mechanisms: thermal – circumstellar matter – stars: winds, outflows – ISM: jets and outflows – ISM: supernova remnants – X-ray: binaries.

1 INTRODUCTION

It is well known that the jets appearing in quasars (Bridle & Perley 1984) and also in the more compact microquasars (Mirabel & Rodríguez 1999) may be considered as the fluid flow emanating from a central source at the jet origin. This approach has been used in the past in order to model quasar jets (e.g. Aloy et al. 1999) and, more recently, microquasar jets (Müller & Brinkmann 2000; Zavala et al. 2008), providing a detailed description of the structure of an astrophysical jet. The jets in quasars are much larger in size, of Galactic scale, and they evolve over thousands of years. On the other hand, *stellar-scale* microquasar jets evolve within the human time-scale, and hence are easier to study in time. However, quasar jets are larger in both observed angular size and actual size, offering better imaging resolution and the possibility of a more refined modelling approach than that for microquasar jets.

A suitable example on which to perform the aforementioned fluid-jet approximation is the SS 433 microquasar system (Begelman et al. 1980; Margon 1984; Spencer 1984; Vermeulen 1993; Fabrika 2004), an X-ray binary comprising a supergiant star and a collapsed stellar remnant. The system has relativistic jets (Margon 1984) which have been studied in various wavelength bands. So far, it is the only microquasar with a definite hadronic content in its jets, as verified from observations of the spectral lines. In more recent observations (Paragi et al. 1999, 2001; Blundell et al. 2001; Spencer 2006; Blundell, Bowler & Schmidtobreick 2008; Doolin & Blundell 2009; Perez & Blundell 2009), two persistent components have been detected in the radio along a direction roughly perpendicular to the main jet of SS 433, which, although weaker than the jet features, appear to occur over different epochs of observation. This equatorial activity has been interpreted as caused by an extended disc, which is presumed to surround the binary at the equatorial plane (Fabrika 1993, 2004; Blundell et al. 2008; Doolin & Blundell 2009; Perez & Blundell 2009). A broad wind originating from the accretion disc (Fabrika 2004) has been assumed (Mioduszewski et al. 2004) as the cause of the equatorial emission, which has been attributed either to thermal (Blundell et al. 2001; Perez & Blundell 2009) or synchrotron (Paragi et al. 2001) radiation mechanisms.

In the vicinity of the binary system, there is a stellar wind from the supergiant companion and also the likelihood of an accretion-disc wind, emitted with a less isotropic distribution (Fabrika 2004; Blundell et al. 2008; Perez & Blundell 2009). The accretion-disc wind is slower and more dense along the equatorial plane, while it is faster and thinner at higher elevations. It is worth mentioning that more recent observations (Fabrika 2004; Blundell et al. 2008; Doolin & Blundell 2009; Perez & Blundell 2009) have led to increased confidence in the presence of a circumbinary disc and to a deeper understanding of its properties.

The aforementioned winds form an environment around the binary in which the relativistic jets may create hydrodynamical effects that influence the equatorial region. The side shocks from the relativistic jet flow may reach the extended disc and create regions of enhanced pressure, temperature and density, which then cause the observed equatorial emission.

In the present work we attempt to model and explore the conditions that are likely to lead to equatorial features similar to those observed in SS 433, assuming that the equatorial emission may be due to a bow-shock–ambient-medium interaction (Smponias 2003, 2006) or alternatively an excretion disc formed from mass loss through a Lagrangian point from the accretion-disc environment (Fabrika 1993). Of course, one may choose a combination of the above effects, e.g. the bow shocks of the jets compressing the wind

★E-mail: hkosmas@uoi.gr

and thus interacting with an excretion disc. We mainly focus on the case of the jet sending shock waves through its surrounding wind, towards the equatorial region, thus causing the corresponding emission.

To a rather good approximation, we adopt a configuration of a denser extended disc along the equatorial region, whereas at higher elevations we introduce a wind with density falling off away from the binary system, in order to describe the wind from the companion star and the relevant component from the accretion disc. Of course, the wind density in the vicinity of the jets might have a more complex distribution; however, for our modelling we adopt a general set-up of a denser flow along the equatorial plane and a thinner wind at higher elevation angles.

2 MODEL SET-UP

In order to investigate the aforementioned mechanism, we set up a hydrodynamic simulation of the SS 433 system, using the PLUTO astrophysical code (Mignone et al. 2007). The jets are approximated as a purely hydrodynamical (HD) relativistic flow. The HD simplification implies that the magnetic field is carried with the flow. Furthermore, the *presumably tangled* field contributes to the coupling of the jet matter that allows the fluid approximation. However, the field cannot affect the dynamics of the flow, as opposed to the magnetic HD (MHD) case in which the field does affect the dynamics.

In practice, it is not always possible to determine from observations whether the HD or the MHD approach is correct for a particular astrophysical jet. Both approaches have been employed in the past for modelling jets (e.g. Müller 1997; Aloy et al. 1999). The HD approach is simpler computationally and in the case of weaker magnetic fields offers an adequately realistic simulation.

The precessing SS 433 jets have hadronic content and their speed is taken as $0.26c$ (Margon 1984), with a precession period of 164 d. In the model, the jets are introduced with the aforementioned velocity value and there is a certain deceleration, as the jet takes around 450 h, or 1.6×10^6 s, of model time to cross the domain of almost 10^{16} cm, whereas at $0.26c$ it would have taken

$$t = l_{\rm domain}/u_{\rm jet}, \quad (1)$$

where

$$t \simeq 10^{16}\,{\rm cm}/(0.26 \times 3 \times 10^{10}\,{\rm cm\,s^{-1}}) \simeq 1.3 \times 10^6\,{\rm s}. \quad (2)$$

Away from the equatorial plane, the wind is represented as a density falling off as $1/r^2$ away from the binary system (r being the distance), although this should be considered as a first approximation to the jet environment. This represents a wind density that decreases as we move away from its source, as expected for a simple constant-velocity mass-conserving stellar wind. Furthermore, the property that the density decreases with the distance from the source is a general configuration for a wind originating from a point in space. The extended disc has a 'velodrome' shape in the model, with a hole in the middle, at the jet base (Fig. 1). The *extended disc* density is also taken to fall off as $1/r^2$ away from its centre, as suggested in Fabrika (1993). The extended disc opening half-angle is set equal to 11.3°. Its density is 1.1×10^7 particle cm^{-3} at a distance of 3×10^{14} cm from the jet base and decreasing outwards.

The model is scaled to fit the Very Long Baseline Interferometry (VLBI) observations of Blundell et al. (2001), Paragi et al. (2001), Blundell et al. (2008), Doolin & Blundell (2009) and Perez & Blundell (2009) (see also Fabrika 1993, 2004), so a size of $45 \times 45 \times 130$ mas^3 was selected for the model space. At the assumed distance of 5 kpc, 1 mas is roughly 0.7×10^{14} cm. At this scale, nevertheless, the size of the binary system will be less than one computational cell and the binary will not be resolved. The wind was assumed to originate from the jet base. The scale of the simulation was therefore much larger than the distance of the binary orbit separation. Both the compact object and the companion star are located in the same computational cell.

Figure 1. A schematic representation of the model system, which comprises the stellar and accretion-disc winds, the jet and the extended disc. The binary is located at the jet base.

Two different combinations of jet and ambient density are tried, providing some insight into how changes in model parameters affect the conditions in the equatorial region (Table 1). The increased influence of the accretion-disc wind in the vicinity of the binary

Table 1. Summary of the hydrocode runs. The ambient density is decreasing proportionally to $1/r^2$, where r is the distance from the jet base. The densities are given for the jet and the ambient medium for each case, in particles (protons) cm^{-3}. The ambient density is given for the jet base, while it decreases further out. The extended disc density also decreases with $1/r^2$ away from the jet base. The disc densities given are for a distance of 2.0×10^{14} cm from the jet base.

Run	Ambient density	Jet density	Ext. disc density
1	10^5	10^6	1.1×10^7
2	10^5	10^4	1.1×10^7

was modelled as a first approximation as a region of increased density near the jet base. The model run is initiated without any preexisting jet, with the jet entering the computational grid from the binary location. The initial jet width is a few computational cells.

The jet densities vary from 10^4–10^6 particle cm^3. The wind densities in the $1/r^2$ case refer to the middle of the eighth cell of the grid after the jet-ejection nozzle, i.e to 10^{14} cm (one code length unit). This density is higher than the expected value for the interstellar medium in the W50 nebula surrounding the SS 433 system, which on average may be around 1 cm^{-3} (Margon 1984; Dubner et al. 1998). The model jet densities are 10 times higher or 10 times lower than the corresponding wind density of each run, not much lighter than the ambient medium, as indicated by the lack of deceleration of the knots on Multi-Element Radio Linked Interferometer Network (MERLIN) scales (Spencer 1984; Vermeulen 1993). A proton jet was assumed for the jet flow, based on optical lines for SS 433 jets (Margon 1984). The values of the model parameters were selected to cover a certain range of ambient and jet densities for SS 433 (Begelman et al. 1980). Some of the simulations were repeated with a wider jet nozzle, which showed no major qualitative differences, only a stronger jet. The shock structures and the cocoon, which interest us the most here, appeared to depend more on the jet velocity and density than on its exact mass output in units of time.

In the $1/r^2$ case the wind density is set by the first cell density. The corresponding range for $(\mathrm{d}M/\mathrm{d}t)/u$ is from 10^8–10^{13} in g cm^{-1}, where u is the wind ejection velocity and M is the wind mass per time dt. For a typical O/B giant stellar companion, mass loss rate of 10^{-6} M$_\odot$ yr^{-1} and wind velocity of 1000 km s^{-1}, the estimate of their ratio seems reasonable: $(\mathrm{d}M/\mathrm{d}t)/u \simeq (10^{-6} \times 2 \times 10^{33}\ \mathrm{g})/(0.3 \times 10^8\ \mathrm{s} \times 10^8\ \mathrm{cm\,s^{-1}}) \simeq 10^{11}\ \mathrm{g\,cm^{-1}}$.

We include in the model an extended disc, thought to emerge from the leakage of material from the binary-system envelope (Fabrika 1993). There might also be a possibility that the jet-wind interaction adds matter to the extended disc, by swapping stellar wind material towards the equatorial plane. However, the case of extended disc formation through wind compression by the bow shocks of the jets can only be modelled in our simulation on a short-term basis. That is because the lifetime of the SS 433 jets is longer than 1000 yr (Spencer 1984), while the model time in the simulations spans a few weeks at most.

Regarding the possibility that the stellar wind constantly replenishes the matter that is swept away by the jet, we see that the jet velocity for SS 433 is 78 000 km s^{-1} as compared with 500–1000 km s^{-1} for the wind. Thus, roughly, the jet velocity is 100 times higher than the wind velocity, $V_{\mathrm{jet}} = 100 V_{\mathrm{wind}}$, so if the wind is to refill a region it must be allowed around 100 times the jet-crossing time of that region before the next outburst. If the region to fill extends out to 2×10^{15} cm then, without considering the jet deceleration, the absolutely minimum jet-crossing time is around 2×10^5 s, or about 2 d. Thus the interburst interval should be at least of the order of 100 d if the wind is to refill the domain. The latter time interval is also compatible with the precession period of the SS 433 jets, which is 164 d, therefore the wind has up to 164 d to fill up a 'hole' in the ambient medium created by the jet before the jet sweeps again by the hole.

The model jets consisted, in all the runs, of ejections of plasmoids (blobs) at regular intervals. Each period of ten code time units (a code time unit equals 3,333 s, or slightly less than an hour of 3600 s) was divided as follows. For four code time units, each blob had an ejection period of 0.3 code time units, followed by a null period of 0.7 code time units. After the above four sequences, a longer null period of six code time units followed. The process resembled a machine gun firing in bursts. During a run, the jets would have completed about $\pi/4$ of precession. This might enhance the equatorial emission, as each time it brings the equatorial emission region closer to a jet. The jet beam was ejected with a small beam-nozzle radius and evolved along its way, depending on the ambient density. The elongated shape of the grid was aimed at accommodating for the motion of the blobs up to a certain extent, before they leave the grid with a free-outflow boundary condition at the end of the grid. The extended disc density was 10^9 cm^{-3} (Fabrika 1993) near the binary system and decreased outwards as $1/r^2$.

The relativistic hydrodynamic (RHD) version of the PLUTO code was used, using three-dimensional Cartesian geometry. The selected algorithm employed the Piecewise Parabolic Method (PPM) (Colella & Woodward 1984). The calculations were performed in parallel on a four-core AMD Phenom II 965 workstation running Linux and using MPI. The data processing was performed using the Vis It visualization package.

The computational grid size was 750 (parallel to the jet axis) by 250 by 250 (directions perpendicular to the jet axis). The corresponding dimensions of the grid were 100 by 35 by 35 in units of 10^{14} cm (the grid cells were not perceived to be entirely cubical). At the presumed distance for SS 433, these correspond roughly to 1.3 mas $= 10^{14}$ cm, i.e. a domain width of nearly 50 mas was employed, scaled as large enough to include the jet and the equatorial emission region. An octant in 3D space was modelled, while the rest of the system was covered, thanks to an assumed symmetry. The model time span of the simulations was of the order of several hundred hours.

3 RESULTS AND DISCUSSION

3.1 Simulations of a jet in a wind

A number of instances are illustrated in Figs 2, 3, 4 and 5, from simulations where the ambient density falls off as $1/r^2$ away from the jet base. It can be seen from these images that the equatorial region appears more active, implying that the equatorial emission may be produced there. A prominent feature in the images is the presence of pressurized entrained material in the equatorial region (see Figs 2 and 3, bottom region). An extended disc was included in the present modelling (Fabrika 1993; see Figs 2 and 3, bottom edge region).

The presence of the stellar wind provides a medium that carries the dynamical influence of the jet towards the equatorial regions. The side shocks of the jets travel through the wind medium and reach the equatorial region and the extended disc, where they heat and activate the local material.

Fig. 2 is a snapshot of the temperature in units of 10^{13} K (a two-dimensional slice of the data space is shown, cut parallel to the jet axis, at 45° azimuth angle) for the heavier jet case, where the jet density (protons per unit volume) was 10^6 cm^{-3} and the ambient density was 10^5 cm^{-3}. The ambient density was decreasing proportionally to $1/r^2$ away from the jet base, modelling a stellar wind construct. This case presents a potential mechanism for the equatorial emission, since there appears to be increased activity in the equatorial region of the system.

Fig. 3 is a snapshot of the temperature in units of 10^{13} K (two-dimensional slice at 45° azimuth angle) for the lighter jet case (jet density 10^4 cm^{-3}, ambient density 10^5 cm^{-3}). This case also presents a potential for equatorial emission, as there is increased activity in part of the equatorial region of the system. The jet cocoon

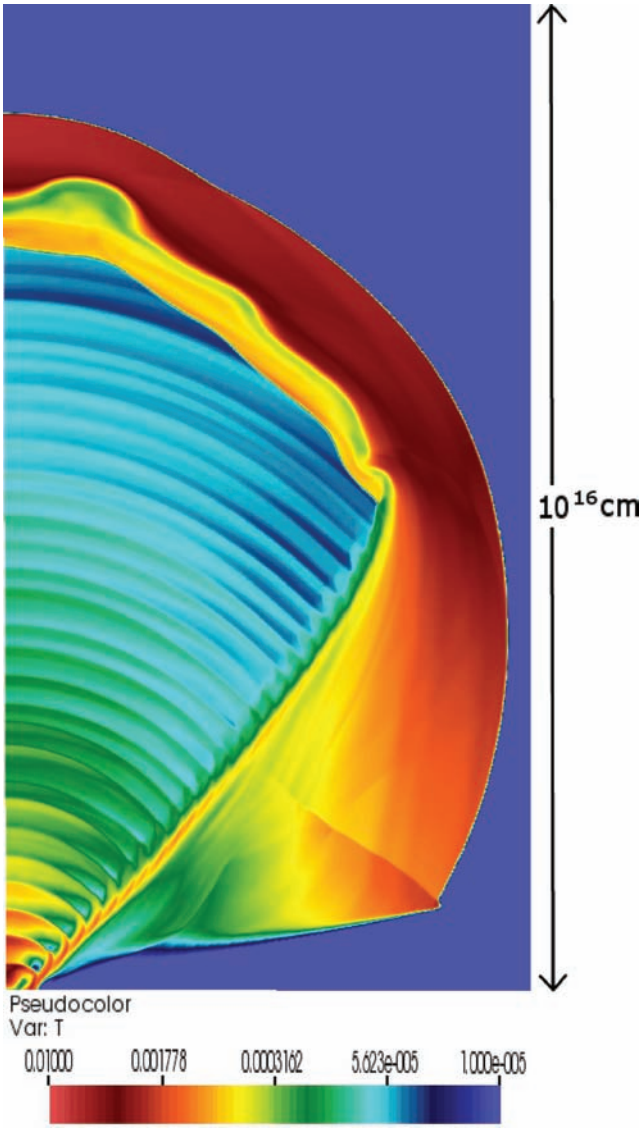

Figure 2. A two-dimensional slice from a three-dimensional simulation, depicting the logarithm of the Temperature T in units of 10^{13} K. The maximum temperature that is plotted is 10^{11} K (the actual maximum is almost the same) while the minimum is 10^{8} K (the actual minimum is near zero). The orientation of the plane of the slice is at 45° azimuth, parallel to the model jet axis. The time instant shown is 400 model time units into the simulation. We can see the equatorial region being heated and activated, as wind matter is swept over by the jet-induced shocks and is 'sandwiched' between the jet effects and the extended disc that is present at the bottom of the image. Multiple shocks appear along the jet, due to successive blob ejections.

is more active now, as the lighter jet makes slower progress through the denser medium.

In Fig. 5 we can see that the surface of the extended disc has become heated after the wind had been swept by the jet side shocks. The side shocks from the jet reach the extended disc, piling up wind matter ahead of them. The combined effect heats the region. After the wind is swept, the hottest parts of the whole system are the jet itself and the equatorial region.

As mentioned above, the jet head advances more slowly than the jet speed and thus causes blobs to strike it periodically from the back, creating a protrusion effect. Subsequent blobs produce their own shocks along the jet, which appear in the the form of stripes along the jet path in Figs 2–5. The blobs also create their individual bow shocks in the area of the jet cocoon. The latter is then a turbulent region in which complex dynamical interactions take place, with oblique shocks and non-linear effects present.

The decreasing ambient density results in a jet that appears more expanded and full-featured, less dense and has more far-reaching effects along the equatorial plane. The latter property means that the jet bow shock moves along the equatorial plane, interacting with both the ambient medium located there and the extended disc. A more thorough discussion of the effects near the equatorial plane is presented below (Section 3.3).

3.2 Features of the model

The hydrodynamic simulations were performed with the aim of testing whether a region of enhanced emission could be induced in the equatorial plane via the introduction of jet bow shocks. The ambient medium on the equatorial plane (see the region directly above the extended disc surface, at the bottom of Figs 2 and 3) is compressed, combined with the presence of the extended disc.

As a result, the ambient medium may be 'sandwiched' on the equatorial plane between the jet-side shocks arriving at it and the extended disc. Thus, an additional jet-induced excretion flow occurs. The reason is that the jet is quite narrow, therefore it pushes ahead a small portion of the stellar wind, while sweeping sideways the majority of the wind matter towards the equatorial region.

The jet head advances in the ambient medium more slowly than the jet flow, at a velocity that depends on the relative jet to ambient matter density ratio (Müller 1997). The detailed morphology at the jet head was relatively well resolved in the simulation runs (see the forefront of the jet expanding towards the top of the computational domain in Figs 2, 3 and 4). The resolution of the jet beamwidth was around 10–20 cells per beam and, as a result, the basic features of a jet did appear in the simulations. The jet bow shock enclosed the backflow and propagated sideways, followed by the bow shocks of successive blobs (in the form of stripes in Figs 2, 3 and 4). This had the effect that the area in the immediate vicinity of the jet trail became very rarefied (along the left side of Fig. 4, which is the jet axis). On the other hand, the stellar wind would have been too slow to refill it.

The active equatorial region could possibly have been more extended due to the effects of jet precession. The jet precesses slowly, covering up to around 45° for the time-scale of the simulation. On the other hand, a precessing jet is situated closer to the equatorial region compared with a straight jet, further enhancing the dynamical effects there.

3.3 The dynamical mechanism of the equatorial emission

A potential mechanism for the emergence of the observed equatorial emission in SS 433 appeared in our hydrodynamical simulations of the SS 433 jets where a $1/r^2$ ambient density distribution was assumed.

Part of the outer jet bow shock (the outer boundary between the jet-shocked region and the still unshocked wind), which is initiated with the appearance of the first blob, propagates sideways from the jet axis (the almost vertical portion of the aforementioned boundary). In both model runs, there was also a small component of the bow shock propagating towards the equatorial plane, due to the ambient density, which decreases with distance. This part of the jet–wind boundary is seen in the bottom right part of Figs 2 and 4, and at the bottom of Fig. 3, as a shock that moves to the

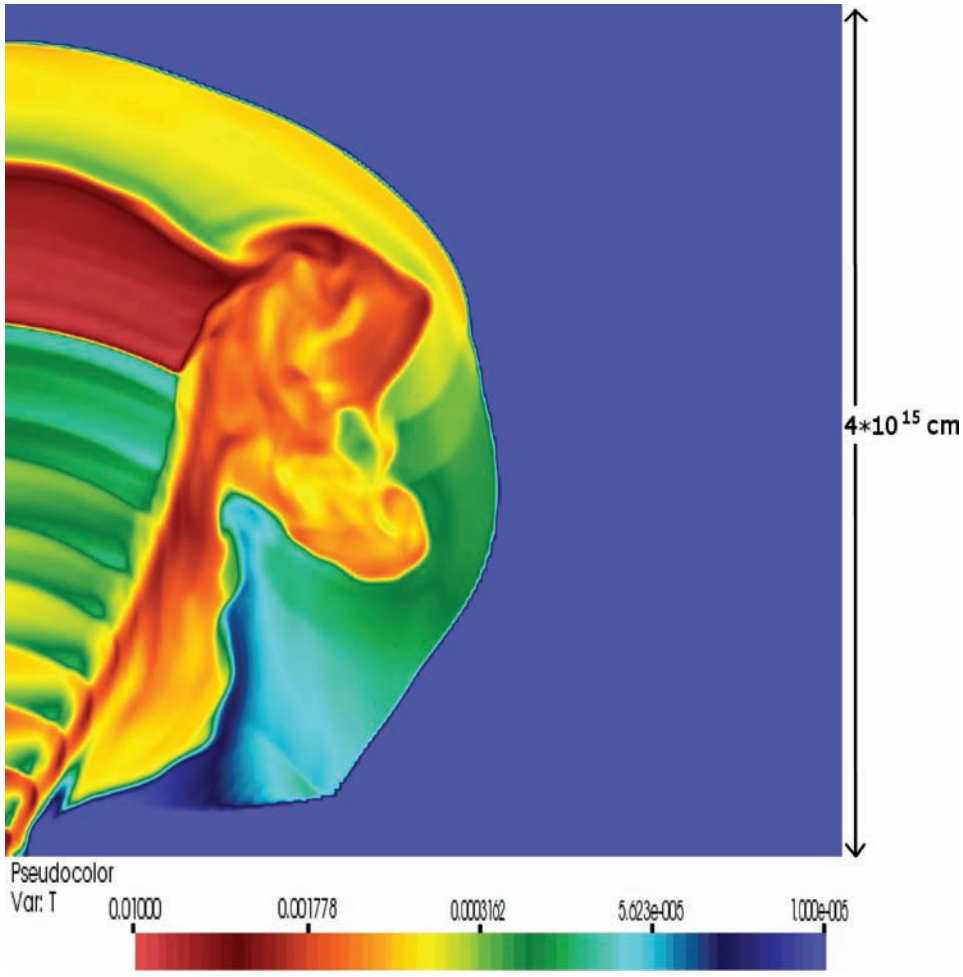

Figure 3. A magnified view (spanning half the width of the computational domain) of a slice at the same orientation, taken at the same model time instance as in Fig. 2, depicting the logarithm of the temperature T for the light jet case, using the same units and value range. The lighter jet now advances more slowly, creating a richer cocoon and a protrusion effect just before the jet head. The equatorial region is also active now, albeit closer to the jet base, and it persists longer due to the slower jet expansion.

right, along the surface of the extended disc, at an angle of less than 90°, i.e. with a component pointing towards the extended disc itself. The latter effect was relatively weak and its appearance may be attributed to the jet expanding faster outwards, where the ambient density drops. Then, a 'half bubble' is formed, which is inflated after a region in which the ambient density becomes smaller. Before the region, the bow shock is still expanding more slowly and with more difficulty through the denser medium. Thus the outer expansion shell has a component of its side-shock velocity parallel to the jet axis and pointing back to the equatorial plane.

Therefore, a possible cause for the equatorial emission is the following. The ambient density does fall along the jet trail, which means that the outer jet's expansion shell is inflated faster than the inner one. This creates an interaction region near the equatorial plane, where a retreating shock from the outer jet (a discontinuity, oriented from top left to bottom right can be seen in Figs 2, 3, 4 and 5, just above the equatorial region), a side shock from the inner jet and matter from the ambient medium coexist (bottom right region in Figs 2 and 4, and bottom region of Fig. 3). Furthermore, as the above areas of activity extend back towards the equatorial plane, they then meet the extended disc.

A mass and energy equatorial concentration appeared to persist in the $1/r^2$ runs of Section 3.1, due to a partly retreating shock from the middle to outer jet region meeting at an angle a slower bow shock from the inner jet region, near the equatorial plane. There, the shock meets the extended disc and an active region appears that persists for some time (bottom right region in Figs 2 and 4 and bottom region of Fig. 3). Later in the modelling, that region was eventually swept over towards the edges of the grid. After that, however, the equatorial area near the surface of the disc was the hottest part of the whole system. The heavier the ambient medium compared with the jet, the more persistent the active portion of the equatorial region, even though it takes longer to form. In the bottom part of Fig. 3, depicting the lighter jet case, the active equatorial region persisted throughout the simulation and even then it was still less than halfway along the surface of the extended disc, on its way towards the side ends of the available grid.

The hydrodynamically active region covered part of the equatorial plane around the compact core. As is apparent in the snapshots from the simulations (Figs 2–5), the location of the active region is above the surface of the extended disc, along the equatorial plane, and therefore compatible with the observations of equatorial emission. The model space had been scaled to be roughly twice the size of the observed equatorial emission features.

The above active regions were expanding slowly, as the horizontally moving side part of the outer bow shock did not advance very

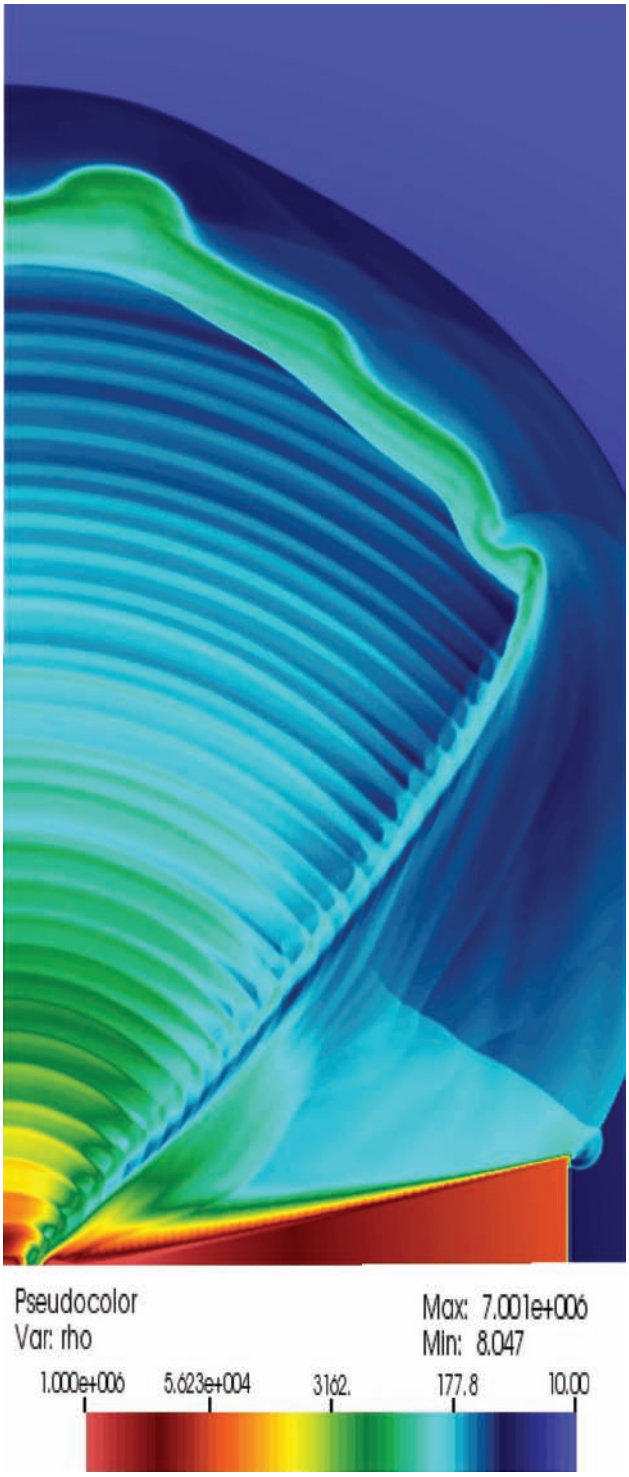

Figure 4. A logarithmic plot of a slice of the density at model time 464, in units of proton cm^{-3}, with the same orientation as the temperature slices. We can see the same pattern at the equatorial region as in the previous images. The domain length along the jet is 10^{16} cm.

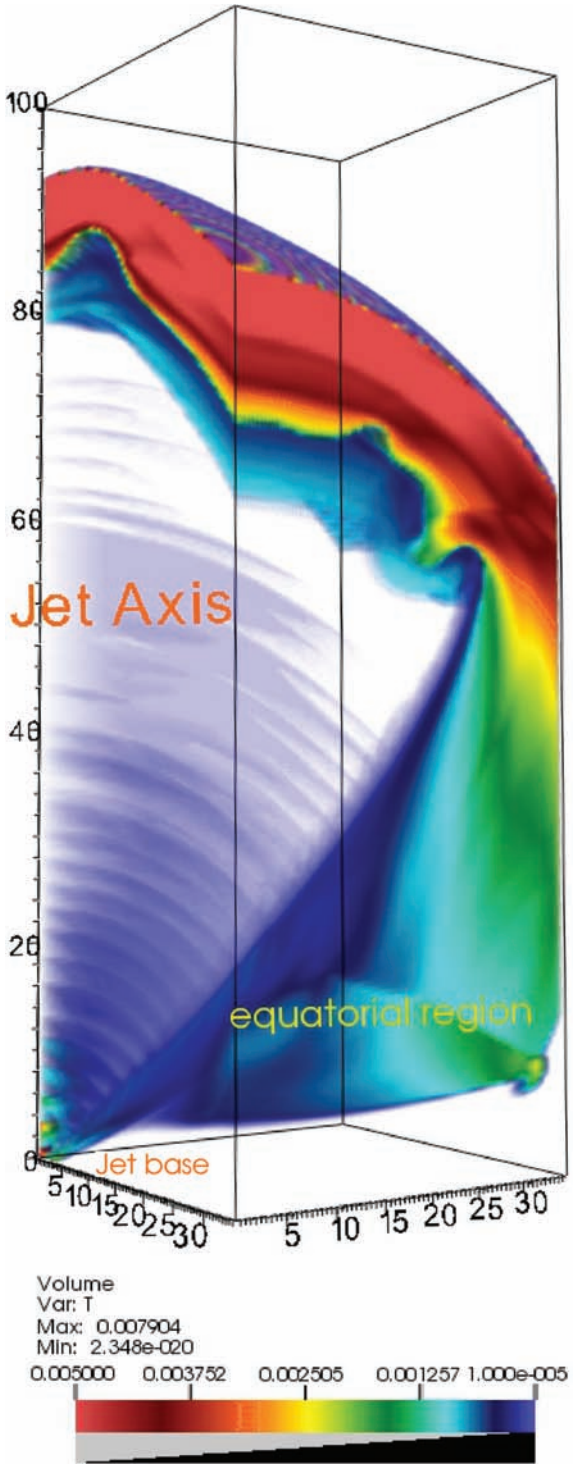

Figure 5. A three-dimensional view of the model system of a heavy jet at model time 464 (around 464 hr), depicting the model octant in 3D space, showing the temperature in code units of 10^{13}K. We can see the same pattern at the equatorial region as in the previous images. The domain length along the jet is 10^{16} cm. The length units along the bounding-box axes are 10^{14} cm.

quickly compared with the jet speed. The presumed reasons for the slowdown are the increasing distance from the jet axis, the pile-up of ambient medium ahead of the expanding active region and the relatively small ratio of jet to ambient density.

For jets heavier than the ambient medium, the first few blobs managed to drill a path through the wind. In the case of lighter jets, however, further blobs are required in order to open a path through the denser inner wind environment.

With lighter jets, the equatorial active region appears more persistent, as the ambient medium is swept less efficiently by a lighter jet. However, a very light jet means that the outer shock never manages to expand fast enough to overrun the inner bow shock considerably

and thus partly retreat and meet it from the side, coming in from the top. An intermediate initial density condition, with ambient density not very much different (i.e. up to 2–3 orders of magnitude at most) from the jet density, provided the best likelihood among our modelled cases for persistent equatorial activity.

3.4 The radiative emission mechanism in the equatorial regions

3.4.1 Theory

In order to calculate the thermal emission from the gas, we integrate the equation of radiative transfer through the three-dimensional volume of the PLUTO computational domain. The emission and absorption coefficients are given respectively by

$$j_\nu = 5.44 \times 10^{-39} g_{\mathrm{ff}(\nu,T)} \frac{n_\mathrm{e} n_\mathrm{i}}{T^{0.5}} \mathrm{e}^{-[h\nu/(kT)]} \quad \mathrm{erg\,s^{-1}\,cm^{-3}\,Hz^{-1}\,sr^{-1}}, \tag{3}$$

$$\kappa_\nu = 0.018 g_{\mathrm{ff}(\nu,T)} \frac{n_\mathrm{e} n_\mathrm{i}}{T^{1.5}\nu^2}\ \mathrm{cm^{-1}} \tag{4}$$

(Rubicki & Lightman 1980; Burke & Smith 2009; Young & Eilek 2009), where n_i and n_e are the ion and electron *number* densities respectively, taken as equal in our case, and given by $\rho_n x_\mathrm{i}$, where ρ_n is the hydrodynamical proton number density and x_i is the ionization fraction.

The Gaunt factor in the radio band is given approximately by (Young & Eilek 2009)

$$g_{\mathrm{ff}(\nu,T)} = 10 \times \left(1.0 + 0.1 \times \log \frac{T^{1.5}}{\nu}\right). \tag{5}$$

In order to facilitate the radiative transfer calculations in technical fashion, the PLUTO code results were regridded to half their original resolution, using PLUTO's attached pload routine. Consequently, the volume of the computational cell to be used in the calculation of the emission coefficient is, at the reduced resolution of 375 cells for 10^{16} cm, around $(10^{16}/375)^3$ cm^3, or about 2×10^{40} cm^3. The distance to the object is taken as 5.5 kpc while no interstellar medium absorption is considered.

For the ionization fraction, we use the Saha equation in a simplified form (Miller 2002):

$$\frac{y^2}{1-y} = \alpha, \tag{6}$$

where

$$\alpha = 4 \times 10^{-9} \frac{T^{1.5}}{\rho} \exp\left(\frac{-1.6 \times 10^5}{T}\right) \tag{7}$$

(all quantities are measured in CGS).

Therefore

$$y_{1,2} = \frac{-\alpha \pm (\alpha^2 + 4\alpha)^{1/2}}{2} \tag{8}$$

and we choose either y_1 or y_2, whichever lies between 0 and 1. We then make a three-dimensional plot of T, ρ vs x_i, and based on that (Appendix A) we use the approximation $x_\mathrm{i} = \min(T^3/10^{14}, 1)$ for the ionization fraction. The latter approximation sets the ionization temperature rather higher than the corresponding theoretical result (see Appendix A) suggests, and this provides an extra margin of reliability for the emission result. In any case, in most parts of the simulation the temperatures are either clearly below the ionization T (pre-shock) or clearly higher (after the shocks).

3.4.2 Results

In Fig. 6 we can see the thermal radio intensity at 8 GHz integrated over the cell emitting volume and over a time period of 1 s. In order for rough comparison with actual observations, we consider a simple application. Let the beam size at the target consist of $25 \times 25 = 625$ image pixels, i.e. that many lines of sight (LOSs; about 9×9 mas). Thus we first multiply an intensity value by that number, to bin average LOSs roughly into 'beams'. Then, let the frequency channel width be 100 KHz at 8 GHz, i.e. multiply the result by a further factor of 10^5. Then, let us take the solid angle cut by a beam at earth, by saying that an antenna of collecting area 100 m^2 contains a beam, therefore $\mathrm{d}\Omega = \mathrm{d}A/(4\pi R^2)$, where R is 5.5 kpc or about 1.7×10^{20} m and therefore $d\Omega$ is about 3×10^{-40} sr. In total, we obtain a multiplication factor of $625 \times 10^{-40} \times 10^5 \times 10^{23}$ (if we express the result in Jy). The result is a factor of 6.2×10^{-10}, which multiplies the value of intensity in the equatorial region. The net result for the intensity is therefore from 10^{-4} to more than 10^{-2} Jy per 'beam', which is generally comparable to a real observation, while the interstellar medium absorption has been left out.

We can see in Fig. 6 that the thermal emission is highest in the jet (especially near its base) and in the bow shock around the jet head. In those regions, high densities of n_i and n_e (we take $n_\mathrm{i} = n_\mathrm{e} = n$) and high T coexist. The emission coefficient is proportional to n^2, while high T is needed to provide the ionization. At the side shock, T is also high enough to provide ionization, although the densities are lower, resulting in reduced emission. In the equatorial region, however, the densities are higher again, though not as high as in the jet head. Thus, equatorial emission does appear with intermediate intensity.

What is more, along the extended disc surface higher densities coexist with high temperatures (Fig. 4), providing increased emission. This is due to the high density of the extended disc, compared with the jet or the wind. The extended disc is set to be much denser but also very cold initially, without thermal ionization. When the jet–wind interaction heats a 'crust' on the extended disc, then the

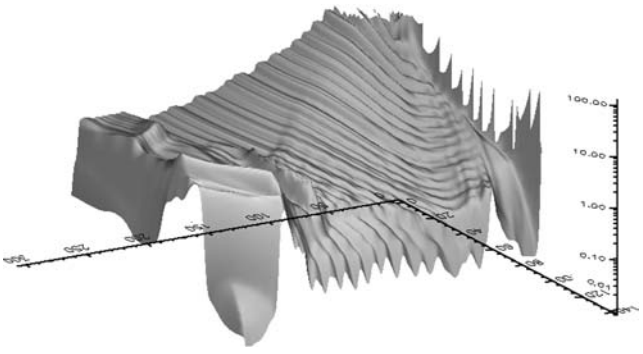

Figure 6. A synthetic view of the thermal radio emission (logarithmic plot) of the heavy jet system at 8 GHz, around model time 450. The value of the intensity has been calculated in units of 10^6 erg Hz^{-1} sr^{-1} per 1 s time interval, i.e. erg sr^{-1} Hz^{-1} s^{-1}. The length units along the bottom plane axes are in radiative code cell lengths of 2.7×10^{13} cm. The jet base is at the top corner, the jet axis is along the top left side and the equatorial region appears slightly above the middle of the top right side. A ridge of locally increased emission there indicates the equatorial emission. A further increase of emission at the side of the jet is seen along the extended disc surface, along the top right side. The extended disc surface emission is even higher (see text for relevant comment), but it has been cut from this figure in order better to resolve the rest of the emissions present.

temperature there rises enough to ionize a portion of the disc surface, allowing for increased thermal emission to occur, combined with the high densities there. This sudden increased emission is in part due to the sharp density jump from the wind to the extended disc, which in reality would have been more progressive. Nevertheless, the presence of the extended disc is indeed able to offer denser material that is heated by jet–wind effects and then emits thermally.

As far as the equatorial region is concerned, along with any previously peaceful region suddenly crossed by the jet shock, the temperature rises by many orders of magnitude. This is seen in the simulation results and may also be justified by a simple order-of-magnitude estimate of the pressure and density there. The pressure is initially set to 10^{-12} in CGS units (Ba), i.e. 10^{-11} Pa, in the simulations. The density, on the other hand, is set to about 10^{-20}–10^{-18} g cm^{-3}. Therefore the initial temperature can be calculated from the equation of an ideal gas, which is used in the code: $T =$ 10–1000 K. The above values are valid initially for the ambient medium at the inner equatorial region, closer to the jet base. After the jet shock passes by, however, the density changes by less than an order of magnitude (due to the jump shock conditions for a non-radiative shock that limit the density increase behind such a moderately relativistic shock to a factor of less than 10) initially, and then by up to a further order of magnitude, thanks to entrainment of matter in the equatorial region for dynamical reasons. The pressure, on the other hand, rises by 9–10 orders of magnitude. Therefore the temperature, which is proportional to the pressure/density ratio, rises by 7–9 orders of magnitude, reaching 10^8–10^{12} K. In the model, we saw an equatorial T of the order of 10^{11} K. Thus we have another indication that adequate conditions for thermal radiation do appear at the equatorial region.

The case of non-thermal emission (Paragi et al. 2001) would need more accurate measurements of spectral index and of polarization in order to be constrained similarly to the thermal emission assumption, as there is not a unique way to calculate non-thermal emission from a given dynamical situation in the system. For the above reason, we first invoked the thermal emission idea (Blundell et al. 2001) in order to approximate the emission from the simulated equatorial dynamics. The model dynamics are indeed able to provide thermal emission in the equatorial region, however non-thermal emission cannot be ruled out based on the modelling alone. The shocked, turbulent equatorial region, as shown in the simulations, may host non-thermal emission.

We shall first estimate and then calculate in more detail the optical depth of the equatorial region in the radio. We use the formula

$$\mathrm{d}\tau = 8.2 \times 10^2 T_\mathrm{e}^{-1.35} \nu_\mathrm{GHz}^{-2.1} N^2 \, \mathrm{d}l \qquad (9)$$

(Mezger & Henderson 1967), where $\mathrm{d}\tau$ is the optical depth and N is the spatial number density of the emitting particles, in particle cm^{-3}. We integrate the above formula over the length $\mathrm{d}l$, along a LOS that crosses the source, and $\mathrm{d}l$ is measured in pc. We choose a characteristic value for T of $T_\mathrm{e} = 10^{11}$ K from the above discussion, $\nu = 5$ GHz, $N = 10^{-18}$ g cm^{-3} (meaning, for protons with a mass of 1.6×10^{-24} g, around 10^4–10^5 particle cm^{-3}) and the length of the LOS is about 10^{15} cm or roughly 10^{-3} pc. The calculation is sensitive to the value of the estimated density in the region, which can vary by an order of magnitude in either direction due to dynamical effects. Then we obtain for the optical depth a value of 10^{-6} for the nominal value, within a possible range of two orders of magnitude above and below, which clearly indicates an optically thin region for the radio emission.

Extending this approximate calculation to the thermal emission in the radio, we can use the approximate formula for the brightness temperature of $T_\mathrm{B} = T_\mathrm{e}\tau$, where T_e is the temperature of the particles in the source and τ is the optical depth. Using the values $\tau = 10^{-6}$ and $T_\mathrm{e} = 10^{11}$ K, we obtain a brightness temperature $T_\mathrm{B} \simeq 10^5$ K. As a result, we can expect a brightness temperature $T_\mathrm{B} \simeq 10^5$, with a margin of two orders of magnitude for each direction. Therefore, at this first approximation, we can still reach the observed temperatures (Blundell et al. 2001, of the order of 5×10^7 K) without invoking non-thermal emission, without of course excluding the non-thermal case.

The density in the equatorial region is distinctly higher as we approach the surface of the extended disc. The above calculation refers to the portion of the equatorial region apart from the disc surface, assuming a maximum density of 10^5 proton cm^{-3}. On the disc, the latter value is exceeded by 1–2 orders of magnitude (see equatorial region in Fig. 4). Therefore, one concludes that without the presence of the disc it is only marginally possible to obtain the equatorial emission thermally, while the presence of such a disc offers even higher densities within its close vicinity. Based on the fact that the aforementioned brightness temperature is proportional to the square of the density, the brightness temperature within the disc influence is at least two orders of magnitude higher and generally compatible with the observations. The model set-up of the disc is a sharp transition from the stellar wind to a dense disc and this is only an approximation. However even this general model set-up shows that there can be an interaction of the jet, wind and disc that further increases the equatorial activity.

The hydrocode results have also been used directly, in order to produce an optical depth map of the simulated region (Fig. 7). This image shows a clearly optically thin region, where the optical depth is higher near the jet base and at the jet shock, however the rather limited dimensions of the absorbing regions prevent it from reaching substantial values, apart from perhaps at the extended disc surface.

As another application, we shall use the formula $L = 2.4 \times 10^{-27} N^2 T^{1/2}$ erg cm^{-3} s^{-1} for the emission in X-rays (Migliari, Fender & Méndez 2002). We therefore have $L = 10^{-11}$ erg cm^{-3} s^{-1}. The assumed source volume is taken roughly as $\pi r^2 D$, with $D = 1.5 \times 10^{14}$ cm and $r = 10D$. Then, $V = 10^{45}$ cm^3 and $L_{\mathrm{x-rays}} = 10^{34}$ erg s^{-1}. We assumed a particle density of 10^6, as seen on the disc surface. Away from the extended disc, the X-ray luminosity result is 2–4 orders of magnitude lower. This result is comparable to the emission in the *Chandra* images (Migliari et al. 2002; Kane

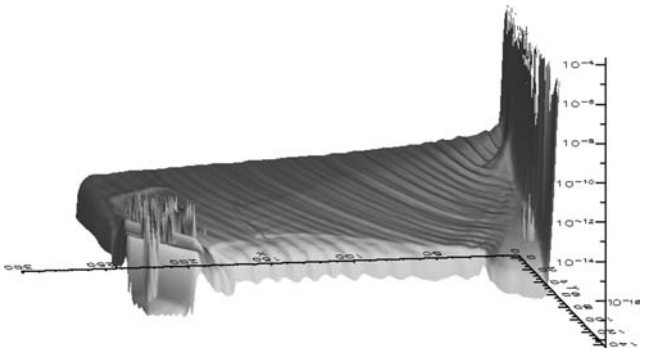

Figure 7. An optical-depth thermal radio map of the heavy jet system at 8 GHz, around model time 450. Most of the jet region and the equatorial region appear optically thin. The bottom plane axis units are in radiative code cell lengths of 2.7×10^{13} cm. The extended disc included in the modelling shows higher values of optical depth, the peaks of which have been truncated from the figure in order to enhance the presentation.

et al. 2002), yet our calculation was only an order-of-magnitude estimate, whereas an argument about non-thermal radiation would require more detailed modelling. Kane et al. (2002) find that the X-ray luminosity at 2–10 keV from the central 1 arcsec region of SS 433 is 3×10^{35} erg s^{-1}. Most of this is from the jets, but an equatorial component at 10^{34} erg s^{-1} may also be present. Thus our model value for the equatorial emission is consistent with those results.

The above results show that the quantities that may lead to equatorial emission are increased in the equatorial region, as a result of dynamical activity, which was one of the main goals of our simulations. There, energy density, pressure, temperature and intensity are higher than before the jet ejections.

4 CONCLUSIONS

The jets in a typical microquasar resembling the SS 433 system have been modelled using ideal gas relativistic hydrodynamics. As appropriate software for this purpose we have employed PLUTO, a three-dimensional hydrocode. The aim of the model was to explore the conditions that may lead to the emergence of the equatorial emission observed in SS 433. It was found that an ambient medium density decreasing with the distance from the jet base, mimicking a stellar wind, may cause the jet bow shock to create an active region at the equatorial plane and cause the observed equatorial emission. A jet of comparable – in terms of order of magnitude – density to the ambient medium produces a more active equatorial region than a much heavier or lighter jet. A very heavy jet meets smaller resistance from the ambient medium even near the jet base, thus the bow shock moves away before an active equatorial region is well-formed. A very light jet should take longer to affect the equatorial region than the duration of an episodic outburst and it was not modelled here.

The presence of a circumbinary disc is likely to enhance the equatorial activity. The reason is that if there is already additional material in the general equatorial region (jet precession would affect that matter in a wider equatorial region) then shocks from the jet find something to hit there and therefore increase the activity further.

The conditions that may lead to enhanced equatorial activity are rather general and quite likely to appear in a microquasar system. The equatorial activity was modelled as a dynamical result of the jet–wind interaction. The case in which an equatorial wind directly causes the equatorial emission, without contribution from the jets, is reserved for a future modelling attempt.

ACKNOWLEDGMENTS

TS wishes to thank Prof. R. Spencer and Dr. T. O'Brien for valuable discussions on jets modelling and Dr E. Vamvakopoulos for technical assistance with MPI. We thank Professor V. Tsikoudi for useful discussions.

TSK wishes to acknowledge support by the Helmholtz International Center (HIC) for Facility for Antiproton and Ion Research (FAIR), HIC for FAIR, within the framework of the LOEWE Program.

REFERENCES

Aloy M. A., Ibáñez J. M., Martí J. M., Gómez J.-L., Müller E., 1999, ApJ, 523, L125
Begelman M. C., Hatchett S. P., McKee C. F., Sarazin C. L., Arons J., 1980, ApJ, 238, 722
Blundell K. M., Mioduszewski A. J., Muxlow T. W. B., Podsiadlowski P., Rupen M. P., 2001, ApJ, 562, L79
Blundell K. M., Bowler M. G., Schmidtobreick L., 2008, ApJ, 678, L47
Bridle A. H., Perley R. A., 1984, ARA&A, 22, 319
Burke B. F., Smith F. G., 2009, An Introduction to Radio Astronomy, 3rd edition. Cambridge Univ. Presss, Cambridge
Colella P., Woodward P. R., 1984, J. Comput. Phys., 54, 174
Doolin S., Blundell K. M., 2009, ApJ, 698, L23
Dubner G. M., Holdaway M., Goss W. M., Mirabel I. F., 1998, AJ, 116, 1842
Fabrika S. N., 1993, MNRAS, 261, 241
Fabrika S., 2004, Astrophys. Space Phys. Rev., 12, 1
Kane J., Marshall H., Schulz N., Canizares C., 2002, American Physical Society, April Meeting, Jointly Sponsored with the High Energy Astrophysics Division (HEAD) of the Amer. Astron. Soc., Meeting ID: APR02, abstract #N17.070, 17070
Margon B., 1984, ARA&A, 22, 507
Migliari S., Fender R., Méndez M., 2002, Sci, 297, 1673
Mezger P. G., Henderson A. P., 1967, ApJ, 147, 471
Mignone A., Bodo G., Massaglia S., Matsakos T., Tesileanu O., Zanni C., Ferrari A., 2007, ApJS, 170, 228, http://www.plutocode.ph.unito.it
Miller C. M., 2002, course notes Astronomy 601, lecture 8. Available at http://www.astro.umd.edu/∼miller/teaching/astr601/lecture8.pdf
Mioduszewski A., Rupen M., Taylor G., Walker C., 2004, NRAO press release, 1100 EST, Monday January 5. Available at http://www.nrao.edu/pr/2004/ss433
Mirabel I. F., Rodríguez L. F., 1999, ARA&A, 37, 409
Müller E., 1998, in Steiner O., Gautschy A., eds, Computational Methods for Astrophysical Fluid Flow: Saas-Fee Advances Course 27: Lecture Notes. Swiss Society for Astrophysics and Astronomy. Springer-Verlag, Berlin
Müller E., Brinkmann W., 2000, in Martens P. C. H., Tsuruta S., Weber M. A., eds, Proc. IAU Symp. 195, Highly Energetic Physical Processes and Mechanisms for Emission from Astrophysical Plasmas. Kluwer, Dordrecht, p. 415
Paragi Z., Vermeulen R. C., Fejes I., Schilizzi R. T., Spencer R. E., Stirling A. M., 1999, A&A, 348, 910
Paragi Z., Fejes I., Vermeulen R. C., Schilizzi R. T., Spencer R. E., Stirling A. M., 2001, Ap&SS Suppl., 276, 131
Perez M. S., Blundell K. M., 2009, MNRAS, 397, 849
Rubicki G. B., Lightman A. P., 1980, Radiative Processes in Astrophysics. John Wiley & Sons, New York
Smponias T., 2003, PhD thesis, Univ. Manchester
Smponias T., 2006, in Solomos N., ed., AIP Conf. Proc. 848, Recent Advances in Astronomy and Astrophysics. Melville, New York
Spencer R. E., 1984, MNRAS, 209, 869
Spencer R., 2006, in Belloni T., ed., Proc. of Science Vol. 33, VI Microquasar Workshop: Microquasars and Beyond. SISSA, Trieste
Vermeulen R., 1993, in Burgarella, D., Livio, M., O'Dea, C., eds, The jets of SS 433, in Astrophysical Jets, Space Telescope Science Institute Symposium Series. Cambridge Univ. Press, Cambridge
Young L., Eilek J., 2009, New Mexico Tech, Course Notes Physics 426, Chapter 4. Available at http://www.physics.nmt.edu/∼lyoung/426/Chap4.pdf
Zavala J., Velázquez P. F., Cerqueira A. H., Dubner G. M., 2008, MNRAS, 389, 1008

APPENDIX A: IONIZATION FRACTION CALCULATION

Based on Section 3.4.1, we produce a plot (Fig. A1) of density versus temperature versus ionization fraction, for a range of ρ from 0–10^{10} cm^{-3} and for T from 0–10^4 K. We can see that ionization takes place at roughly a few times 10^3 K, and that this temperature changes rather slowly with density. Therefore, we adopt the approximation of

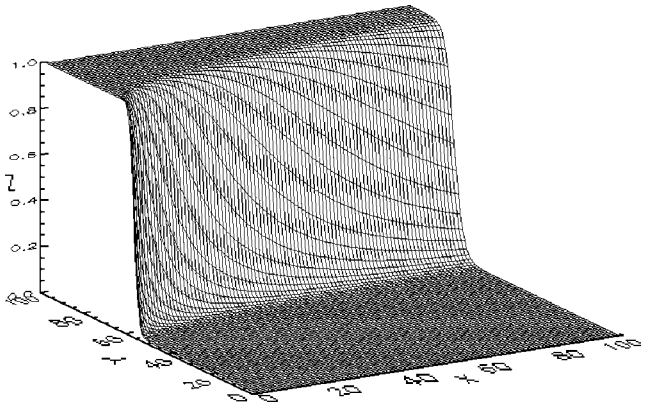

Figure A1. A plot of the ionization fraction (z axis) against the square root of the temperature (y axis) and the fifth root of the density (x axis). The temperature ranges from 0–10^4 K, while the density range is from 0–10^{10} g cm^{-3}.

Section 3.4.1 for the ionization fraction, which implies an ionization temperature of around 2×10^4 K, an order of magnitude more than the actual ionization, providing an extra margin (Section 3.4.1).

APPENDIX B: LINE-OF-SIGHT INTEGRATION

B1 In two dimensions

In two dimensions, the LOS code works as follows. The rectangular domain is divided into a number of discrete cells, each of which holds a set of values for hydro quantities such as density, pressure, etc. We begin at a point (x_0, y_0) at the bottom side of the rectangular domain (Fig. B1). We are allowed to move either a step right or a step up in the discrete grid. Our purpose is to follow the actual LOS as closely as possible. After each such step, we compare the quantity $(y - y_0)/(x - x_0)$ with $\tan(\theta)$. If $\tan(\theta)$ is larger, then our next step is up. Otherwise, the next step is to the right. In this manner we stay close to the LOS until we exit the grid. The actual length of the LOS, $[(y - y_0)^2 + (x - x_0)^2]^{-1/2}$, is divided by the number of its cells, in order to account for the increased path length due to crossing the domain in a non-straight line. Along the way, the properties of the elements of the LOS are stored in a corresponding one-dimensional array. Using a one-dimensional loop for the base of the rectangle, this process is repeated for every starting point along the base, resulting in a one-dimensional 'image' of the domain base, each point of which has its own LOS crossing it.

During the above, we only consider radiation travelling along the LOS, originating from and absorbed solely by elements of the LOS. We assume emission and absorption only along the LOS.

B2 In three dimensions

The above process is repeated also in the 3D case, only there we have two angles, azimuth and elevation, for a parallelepiped domain. The bottom of the grid is now two-dimensional, and for each one of its points a LOS is drawn.

We start at a point towards the 'left' (in the sense that the LOS aiming angles are allowed to vary from 0 to $\pi/2$) of the base of a rectilinear grid, i.e. $x = x_0, y = y_0, z = z_0$. Then, we define the values of two angles that characterize the LOS direction, $\phi_{1\mathrm{f}}$ and $\phi_{2\mathrm{f}}$, as a target for the LOS (f stands for final angle, as opposed to current angle). ϕ_1 gives the azimuth angle and ϕ_2 is the elevation.

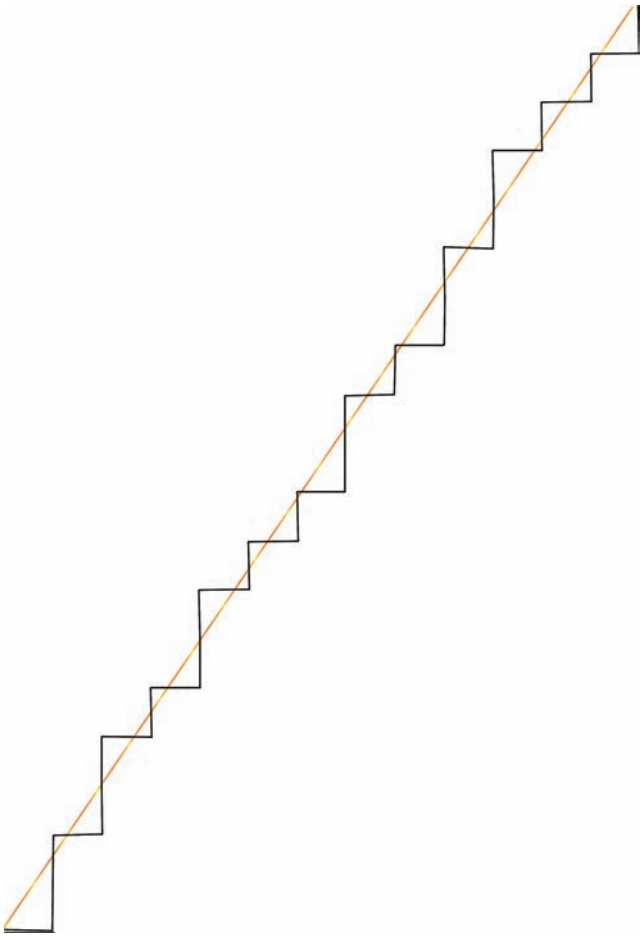

Figure B1. The LOS course through a two-dimensional discrete domain. The straight line is the actual continuous LOS, while the computational LOS follows it through the grid points. The length of the LOS then increases, but this is accounted for in the code.

Then the code starts advancing in the discrete grid, in either x (r: right), y (u: up) or z (c: climb). In order to follow the LOS closely within the discrete grid, there are two if–then–else criteria.

For $\tan(\phi_1)$: if (current) $\tan(\phi_1)$ is less than $\tan(\phi_{1\mathrm{f}})$ then step up (u), else step right (r).

For $\tan(\phi_2)$, where $\tan(\phi_2) = z/[\sqrt{(x^2 + y^2)}]$: if $\tan(\phi_2)$ is less than $\tan(\phi_{2\mathrm{f}})$ then increase z (c: climb), else increase x or y. To determine which, use again the first criterion.

For each one of the above steps, the LOS advances one cell, therefore we count two cells in total for each loop iteration. We always update the LOS arrays after every grid step. The values of each selected point of the 3D grid is assigned as the next point of the LOS vector. As the number of elements of the LOS increases, we get closer to the desired LOS, till we finally reach the ends of the grid. For SS 433, the LOS direction angle ϕ_1 takes a value of 79° to the jet precession axis, while in our case $\phi_2 = 0$.

B3 Radiative transfer

For each domain point along the LOS, we use the equation of radiative transfer:

$$\mathrm{d}I_\nu = -I_\nu k'_\nu + \epsilon'_\nu, \tag{B1}$$

where I_ν is the intensity arriving from the previous LOS segment (I is set to zero initially) and k'_ν and ϵ'_ν are the absorption and emission

coefficients respectively. These are related to the corresponding coefficients of equations (3) and (4) through the following relations:

$$k'_\nu = k_\nu \times \mathrm{d}l' \tag{B2}$$

and

$$\epsilon'_\nu = \mathbf{J}_\nu \times \mathrm{d}V \times \Delta\nu \times \mathrm{d}t \times \mathrm{d}\Omega, \tag{B3}$$

where $\mathrm{d}l'$ is a 'normalized' radiative computational cell length of

$$\mathrm{d}l' = \mathrm{d}l \times \frac{L_{\mathrm{LOS}}}{N_{\mathrm{LOScells}}}, \tag{B4}$$

where

$$L_{\mathrm{LOS}} = [(x - x_0)^2 + (y - y_0)^2 + (z - z_0)^2]^{1/2} \tag{B5}$$

is the LOS length in units of cell length, x, y and z are measured in dimensionless numbers of cells and N_{LOScells} is the number of cells along a given LOS and is computed by the radiative code.

The aforementioned parameter values are $\mathrm{d}l = 2.7 \times 10^{13}$ cm (twice the size of a PLUTO cell due to the regridding performed), $\Delta\nu = 100$ kHz, $\mathrm{d}t = 1$ s and $\mathrm{d}\Omega = 3 \times 10^{-40}$ sr (Section 3.4.1).

Further on, we integrate the equation of radiative transfer (B1) along the LOS, and this is repeated for every LOS, one for each point of the domain base. The quantities of density and temperature are provided by the hydrocode.

This paper has been typeset from a TEX/LATEX file prepared by the author.